PCCP

ROYAL SOCIETY OF CHEMISTRY

PAPER

View Article Online
View Journal | View Issue

Cite this: *Phys. Chem. Chem. Phys.*, 2026, **28**, 6388

A comparative study of the lattice dynamics of alkali titanium hexahalides

Junbiao Guo, [a] Keith Refson [b] and Martin T. Dove *[acd]

Received 22nd October 2025,
Accepted 16th February 2026

DOI: 10.1039/d5cp04058b

rsc.li/pccp

Lattice dynamics calculations have been performed on a family of vacancy double perovskites of general formula A_2TiX_6 (A = Rb, Cs, X = F, Cl, Br, I) using density functional theory. This family has attracted interest as potential lead-free optoelectronic materials with tuneable band gaps. We find that most of these materials show stable lattice dynamics, but two, Rb_2TiF_6 and Rb_2TiI_6, show instabilities which would lead to a phase transition. In fact Rb_2TiF_6 normally crystallises in a phase with a different structure, which can be understood on the basis of calculations of the free energy.

1 Introduction

Among the materials used in solar cells, lead-based perovskites show relatively high efficiencies. However, these are not suitable for large-scale applications due to their toxicity and instability.[2,3] One approach is to replace lead with tin or germanium, elements from the same group in the periodic table. But they too are chemically unstable, because the Sn^{2+} + and Ge^{2+} ions are easily oxidised to Sn^{4+} and Ge^{4+}. Furthermore, tin is also harmful to the human body.[4,5]

Currently, there is a concentrated search for lead-free perovskites or perovskite derivatives as alternatives. One potential family of materials is the so-called vacancy double perovskites, with chemical formula of A_2BX_6 (A = K, Rb, Cs, *etc.*, B = Se, Ti, Pd, Mn, *etc.*, X = F, Cl, Br or I). The introduction of halide anions can adjust the band gap by altering the electronic band structure of the material, thereby influencing its optoelectronic properties.[6–11] This structure is similar to the normal double perovskite, of general fomula $A_2B'B''X_6$, where the B″ cations are replaced by vacancies. These structures have the cubic space group $Fm\bar{3}m$.[12] The group IV element titanium exists in a stable tetravalent state in these materials, it has a good biocompatibility, and it is abundantly available. The A_2TiX_6 vacancy double perovskites hold promise as substitutes for traditional $APbX_3$ perovskites, while maintaining a high conversion efficiency.[13,14] The crystal structure of the vacancy double perovskites A_2TiX_6 with the space group of $Fm\bar{3}m$ is shown in Fig. 1. The structure is composed of unconnected TiX_6 octahedra on the lattice sites, with A atoms filling the spaces between the octahedra. The point half way between lattice sites along the unit cell edges, a vacant site with halide neighbours, is the site that would contain a cation in the standard perovskite or double perovskite structures.

A number of recent papers have reported on the experimental synthesis of various A_2TiX_6 crystals, and others have reported density functional theory (DFT) calculations.[20–24] The experimental studies have shown that not all elemental combinations can be synthesised, and in some cases the compounds crystallise in a different space group, such as the trigonal $P\bar{3}m1$.[25,26] Most DFT calculations tend to focus on electrical

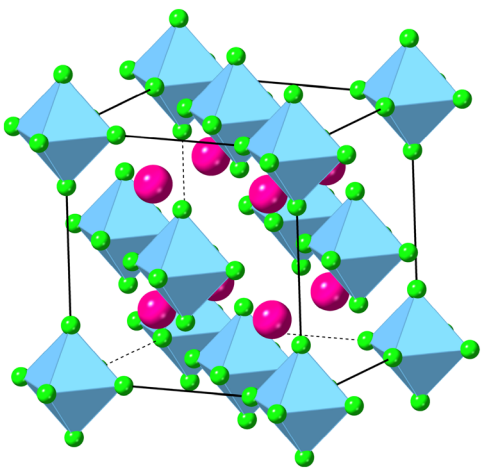

Fig. 1 Crystal structure of A_2TiX_6 (A = Rb, Cs, X = F, Cl, Br, I). The big pink spheres and small green ones denote A and X atoms, respectively. The blue octahedra combined with green spheres represents TiX_6. The figure was drawn using CrystalMaker.[1]

[a] *Institute of Atomic and Molecular Physics, Sichuan University, Chengdu, Sichuan 610065, China. E-mail: martin.dove@icloud.com*
[b] *ISIS Facility, Harwell Campus, Chilton, Didcot, OX11 0QX, UK*
[c] *School of Mechanical Engineering, Guizhou University of Engineering Science, Xueyan Road, Bijie, Guizhou, 55170, China*
[d] *School of Physical and Chemical Sciences, Queen Mary University of London, Mile End Road, London, E1 4NS, UK*

and optical properties, and calculations of lattice vibrations have broadly been neglected. Careful lattice dynamics calculations, comparing known synthesized compounds with those that have not yet been synthesized, help to improve our understanding of stability, and can improve the efficiency of the search for new materials by evaluating the likely stability of any candidate material. Moreover, there are some compounds that can be successfully crystallised, but unfortunately their stability in the environment is questionable. For example, Cs_2TiBr_6 has been studied, with some research using DFT to calculate its electronic, optical, and thermal properties, indicating that this halide perovskite could be a promising optoelectronic material.[27,28] But there is some debate as to whether it decomposes in standard environments.[29–31] Such experiments have also been conducted for Cs_2TiCl_6, and this material seems much more stable than the bromide counterpart.[21]

From this discussion it would seem that there is an important role for lattice dynamics calculations in these materials. In this paper, we have selected A_2TiX_6 (A = Cs or Rb, X = F, Cl, Br or I) compounds for DFT calculations, focusing on the impact of lattice dynamics on the stability of these perovskite materials. We have found from our lattice dynamics calculations that while some certain compounds may potentially have exciting electrical, optical or thermoelectric properties, they are, in fact, unstable, or may experience a phase transition. Additional calculations, including the Goldschmidt tolerance factor and an analysis of possible space groups induced by soft modes, are also performed to supplement the main results.

2 Methods

The calculations were performed using the CASTEP software, with plane waves representing the electronic states.[32] Norm-conserving pseudopotentials, provided by the NCP19 library in CASTEP, were used to handle the core electrons. For the simulation of A_2TiX_6 (A = Cs or Rb, X = F, Cl, Br or I), the PBE generalised gradient approximation (GGA) was employed.[33,34] A $5 \times 5 \times 5$ Monkhorst–Pack grid[35] of wave vectors was selected, and cut-off energies ranging from 800 to 1300 eV were used for different A_2TiX_6 compounds based on convergence tests.

For geometry optimisation, the convergence tolerance for accepting free energy, force, stress, and ionic displacement were set as 10^{-6} eV per atom, 5×10^{-3} eV Å^{-1}, 10^{-2} GPa, and 10^{-4} Å, respectively.

Phonon calculations were performed using density functional perturbation theory (DFPT), and the interpolation method was applied to compute the frequency for different wave vectors within the Brillouin zone.[36,37] A $5 \times 5 \times 5$ Monkhorst–Pack grid was employed for calculating the dynamical matrix for interpolation to other wave vectors, which internally within the program sets the range of neighbouring unit cells used for the contribution of distance interactions to the dynamical matrix. The acoustic-sum-rule correction was used to ensure that the frequencies of the acoustic modes tend towards zero value for wave vectors around the Γ point in the Brillouin zone (zero wave vector).

Elastic constants were calculated by fitting the stresses calculated when a range of different strains were imposed on the relaxed crystal structure.

3 Results

3.1 Crystal structure

The calculated values of the lattice parameter a are compared with experimental data and the results of previous calculations in Table 1. Most of the calculated values match well with those of prior calculations or experimental data, with the maximum difference between calculations and experiments being 3.6%. As we will discuss later, from the lattice dynamics calculations Rb_2TiF_6 and Rb_2TiI_6 appear to be unstable in the cubic structure.

3.2 Elasticity

For a cubic system, there are only three independent elastic constants C_{11}, C_{12} and C_{44}. Their calculated values, together with the bulk modulus $K = (C_{11} + 2C_{12})/3$, are given in Table 1. There is an apparent trend that the values of all coefficients systematically decrease with the increase of the masses and ionic radii of both the alkaline cation and the halide anion.

3.3 Phonon dispersion curves

Dispersion curves of the eight compounds A_2TiX_6 (A = Cs, Rb, X = F, Cl, Br, I) in space group $Fm\bar{3}m$ are presented in pairs in Fig. 2 and Fig. S1–S3 (shown in the SI). The irreducible representations of the three acoustic modes are the triple-degenerate T_{1u}, and the decomposition of the 24 optic modes at Γ point (zero wave vector) are the irreducible representations $A_{1g} + E_g + T_{2u} + 2T_{2g} + 3T_{1u} + T_{1g}$. There is a LO/TO splitting

Table 1 Calculated structure data and elastic constants for vacancy double perovskites A_2TiX_6

Formula	a (Å) (This study)	a (Å) (Other calc.)	a (Å) (Exp)	Ti–X (Å) (This study)	C_{11} (GPa) (GPa)	C_{12} (GPa) (GPa)	C_{44} (GPa)	K (GPa)
Rb_2TiF_6 (unstable)	8.84	—	—	1.886	27.59	12.56	7.21	17.57
Rb_2TiCl_6	10.26	10.27[15]	10.01[16]	2.362	22.42	7.38	5.82	12.39
Rb_2TiBr_6	10.82	10.95[15]	—	2.535	23.35	5.63	6.15	11.54
Rb_2TiI_6 (unstable)	11.63	11.95[17]	—	2.774	18.71	5.84	4.06	10.13
Cs_2TiF_6	9.27	10.10[9]	—	1.889	24.48	11.98	6.16	16.15
Cs_2TiCl_6	10.60	10.62[18]	10.23,[16] 10.24[19]	2.365	18.51	6.50	4.85	10.50
Cs_2TiBr_6	11.10	11.08[18]	10.92[13]	2.538	17.13	5.50	4.33	9.38
Cs_2TiI_6	11.83	11.88[18]	11.67[13]	2.779	16.30	4.73	3.98	8.59

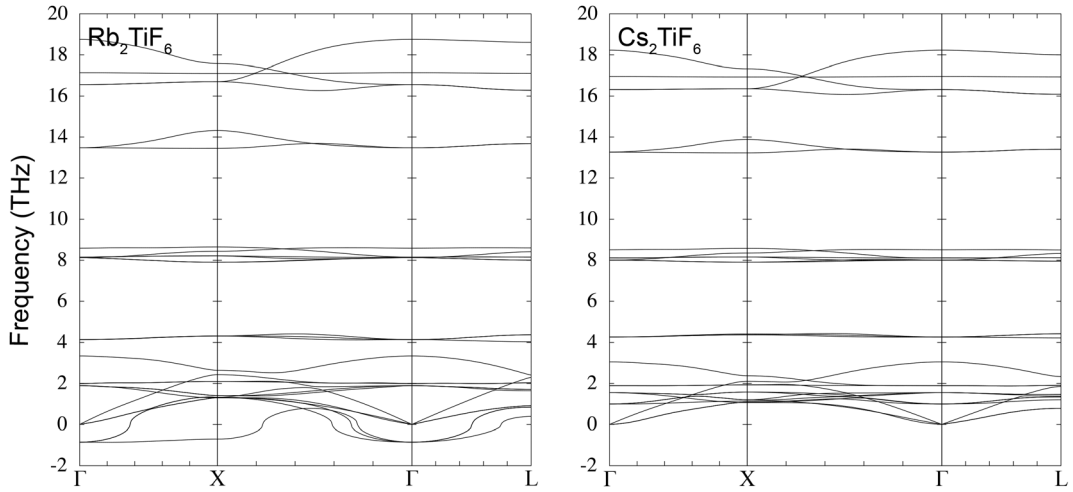

Fig. 2 Phonon dispersion curves of Rb_2TiF_6 (left) and Cs_2TiF_6 (right) in the space group of $Fm\bar{3}m$. The wave vectors lables are Γ = [0, 0, 0], X = [0, 0, 1] and L = [1/2, 1/2, 1/2]. Negative values indicate imaginary values, from the fact that the calculated frequency-squared values are negative.

around Γ in all of the dispersion curves, which affects the three optic T_{1u} modes by splitting into singlet and doublet modes, $3(E_u + A_{2u})$. The dispersion curves show a number of general trends. In each case the highest six frequencies are the Ti–X stretching modes, which, considering the linear X–Ti–X linkage, are either symmetric ($E_g + A_{1g}$) or asymmetric (T_{1u}) with regard to the octahedral centre of symmetry. In each case the longitudinal asymmetric stretch mode has highest frequency. Immediately below the stretch modes are the nine modes involving bending of the bonds within the TiX_6 octahedra ($T_{2u} + T_{2g} + T_{1u}$). At yet lower frequencies are the six modes involving the displacements of the A cations and the whole-body TiX_6 octahedra ($T_{2g}+ T_{1u}$). Finally, at the lowest frequencies, are the three modes involving rotations of the TiX_6 octahedra (T_{1g}), which have some interesting features we will discuss below. Representations of these mode eigenvectors are given through the example of Cs_2TiI_6 in Fig. S4 and the list of Γ point frequencies is in Table S1 (given in the SI).

The trends in the frequencies are shown in cartoon form in Fig. 3. In every case, with increasing frequency, the groups of frequencies are the displacement, bond-bending and bond-stretching modes, with no significant overlap. The ranges of frequencies are nearly the same for A = Rb and A = Cs, which is not at all surprising for the bond-bending and bond-stretching modes because these involve only minimal or no displacements of the A cations. For the displacement modes, we might expect the mass difference (ratio of 85.5 : 132.9 for Rb : Cs) to give higher frequencies for A = Rb than for A = Cs. This is sometimes seen to be the case, as in the case X = F, but not always. The most striking visual impression from Fig. 3 is the effect from the mass of the X anion. With increasing mass the frequencies of the bond-stretching and bond-bending modes fall considerably, with an effect also on the displacement modes.

It is the low-frequency TiX_6 rotational modes that do not obviously follow an exact trend with mass. From Fig. 2 and Fig. S3, Table S1, it can be seen that the rotational modes for

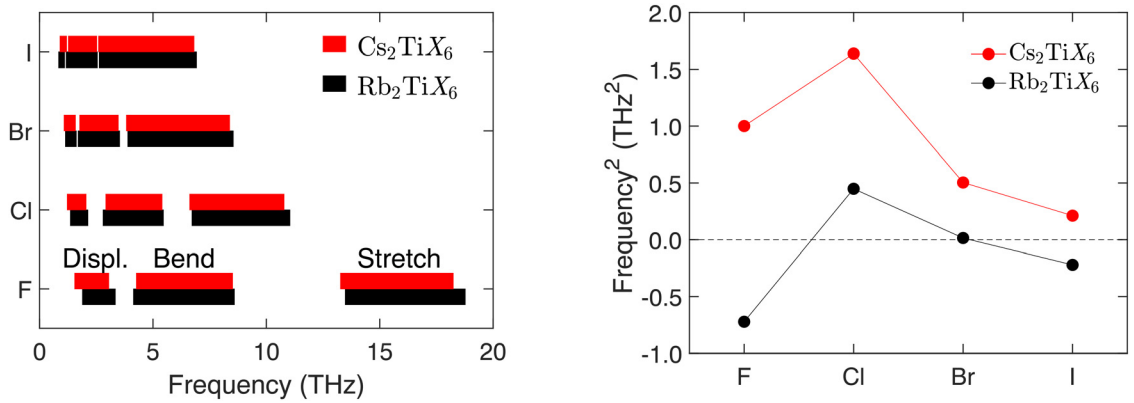

Fig. 3 Left is the representation of the ranges of frequencies of the three main types of vibration in A_2TiX_6, namely the modes involving Ti–X stretching, X–Ti–X bending, and displacements of the A cations and TiX_6 octahedra. Red and black represent the two cases A = Cs and A = Rb, respectively. The results for the four halogens are displaced vertically. Right is the squares of the frequencies of the TiX_6 rotational modes at the Γ point for the range of X anions, and plotted separately for the Rb and Cs as A cations. Negative values indicate unstable modes.

Rb_2TiF_6 and Rb_2TiI_6 in space group $Fm\bar{3}m$ show instabilities, in that the frequencies have imaginary values (negative values of the squared frequencies obtained by diagonalisation of the dynamical matrix). The squared frequency values for the range of materials are plotted in Fig. 3. It can be seen that the cases A = Rb and A = Cs follow the same basic trends, with X = Cl having the highest squared frequencies in both cases, with the squared frequencies decreasing on increasing mass from Br to I. Moreover, from Table 1 we see that there is a corresponding increase in the the Ti–X bond lengths, with both effects leading to an increase in the moment of inertia of the TiX_6 octahedra. The big surprise is that the case X = F breaks the trend in both cases, having much lower squared frequencies rather than an increase in value. This is not immediately easy to understand. Similarly it is not easy to understand why the frequency-squared values for Cs_2TiF_6 are systematically higher that for Rb_2TiF_6, given that the A cation does not contribute to the mode eigenvectors. With a larger unit cell, and larger A–X distances, one might have expected that the potential energy associated with rotations of the TiX_6 octahedra would be seen as softer, yet the opposite appears to be the case.

It is interesting to note that the instabilities seen in the phonon dispersion of Rb_2TiF_6 and Rb_2TiI_6 for the rotational modes show very similar characteristics. Both show softening all across the branch from Γ–X along the [100] direction, but in the other two symmetry directions, Γ–X along the [110] direction, and Γ–L (along the [111] direction), the instabilities are confined to wave vectors close to Γ. Given that A_2TiX_6 is a double perovskite with one octahedral site vacant, the interesting point is that the soft [100] direction with a triple degeneracy at Γ directly reflects the low energy branches of rigid unit modes in cubic single perovskites.[38–40] In fact the triple-degenerate mode splits into a singlet state which stays soft along the line, and a doublet mode that increases in frequency, as seen in perovskite. This is seen in all compounds, but as we have discussed, the degree of softening of this mode is different for each compound (Fig. 3).

It is known that the compounds Rb_2TiF_6 and Cs_2TiF_6 crystallise in a trigonal structure of space group $P\bar{3}m1$.[25,26,41] This symmetry is not a subgroup of $Fm\bar{3}m$, and therefore there will not be a displacive phase transition between the two structures. Thus the existence of the trigonal phase is not directly related to the instability seen in the rotational mode in Rb_2TiF_6 (and this mode is not unstable in Cs_2TiF_6, although it does have a low frequency). We present calculations of the phonon dispersion relations of Rb_2TiF_6 and Cs_2TiF_6 in space group $P\bar{3}m1$. Broadly we see similar patterns of the branches if we compare the results shown in Fig. 4 with those of the cubic $Fm\bar{3}m$ structure, Fig. 2. We see the same distributions of bands for the stretch, bending and displacement modes. However, it is clear that in the $P\bar{3}m1$ structure the rotational mode is quite stable, and in Cs_2TiF_6 it has a higher frequency than in the cubic phase.

3.4 Phonon contributions to thermodynamic properties

We now turn our attention to the question of the relative stabilities of the $Fm\bar{3}m$ and $P\bar{3}m1$ phases of Cs_2TiF_6, based on the evaluation of the overall free energy $G = H - TS$, where the symbols have their usual thermodynamic meaning. The phonon contribution to the free energy is obtained from the phonon frequencies using standard equations from statistical mechanics.

The phonon density of states has been evaluated from calculations for 10 000 wave vectors spread randomly throughout the whole Brillouin zone, and results are shown in Fig. 5. The consistency with the phonon dispersion curves for symmetry directions, Fig. 2, is clear, particularly with regards to the gaps around 6, 10 and 15 THz. There are some small differences between the two sets of dispersion curves, notably in the external region from 0–3 THz, and in the bending regions at around 5 THz and 7.5 THz. These may have an influence on the differences in phonon free energy.

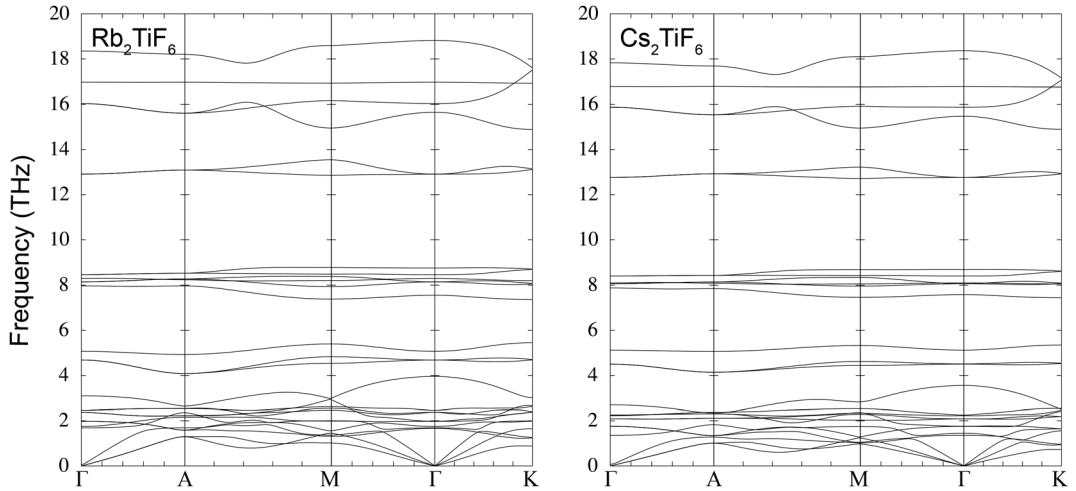

Fig. 4 Phonon dispersion curves of Rb_2TiF_6 (left) and Cs_2TiF_6 (right) in the space group of $P\bar{3}m1$. The wave vectors lables are Γ = [0, 0, 0], A = [0, 0, 1/2], M = [1/2, 0, 0] and K = [1/3, 1/3, 0].

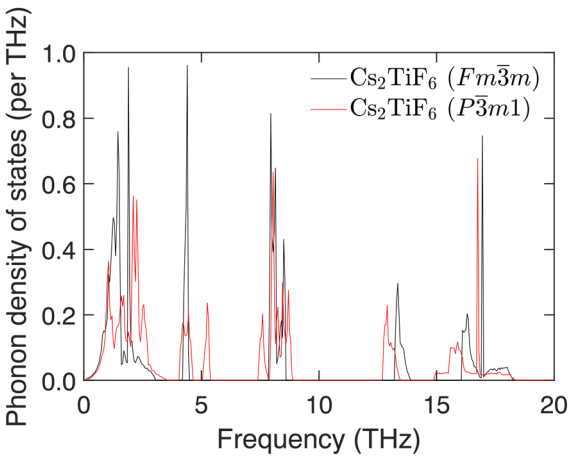

Fig. 5 Phonon density of states of Cs_2TiF_6 in two phases.

The phonon free energy of the two phases of Cs_2TiF_6 are compared in Fig. 6. At 0 K the phonon free energy for the $Fm\bar{3}m$ phase is 0.05 kJ mol^{-1} below that of the $P\bar{3}m1$ phase, and on increasing temperature the phonon free energy of the $Fm\bar{3}m$ falls faster. This corresponds to having a higher entropy, coming from the balance of the external phonon modes (0–3 THz) having a higher density at lower frequencies in the density of states, Fig. 5. The lattice energy itself certainly favours the $Fm\bar{3}m$ phase over the $P\bar{3}m1$ phase, with the former having an energy 4.747 kJ mol^{-1} below that of the latter. The relative free energy is also shown in Fig. 6. It is clear from this analysis that the $Fm\bar{3}m$ phase is the stable phase of Cs_2TiF_6 over all temperatures, leading to the conclusion that the $P\bar{3}m1$ phase is crystallised as a metastable state.

In the case of Rb_2TiF_6, however, because some of the phonons are unstable in the $Fm\bar{3}m$ phase, we cannot obtain the corresponding comparison of phonon free energy. However, because of the similarities of the general features of the phonon spectra, we might anticipate from comparison with Cs_2TiF_6 that at temperatures high enough to stabilise the phonons in Rb_2TiF_6, the entropy of the $Fm\bar{3}m$ phase will also be higher than that of the $P\bar{3}m1$. On the other hand, from the lattice energy calculations we find that the energy of the $P\bar{3}m1$ phase is 4.134 kJ mol^{-1} lower than that of the $Fm\bar{3}m$ phase. Thus certainly at lower temperatures the stable structure of Rb_2TiF_6 is predicted to be that of the $P\bar{3}m1$ phase, and from comparison with Cs_2TiF_6 (Fig. 6) we anticipate that the difference in phonon free energy is unlikely to drive a phase transition at any practical temperatures.

3.5 Goldschmidt tolerance factor

The Goldschmidt tolerance factor[43] t is a geometric criterion used to assess the structural stability of classical perovskite ABX_3 compounds,[44] and it can be extended to vacancy double perovskite A_2BX_6 in this study. Together with another geometric factor, the octahedral factor[45] μ, these two are defined as $t = (r_A + r_X)/(\sqrt{2}[r_B + r_X])$ and $\mu = r_B/r_X$, where r_A, r_B and r_X are the effect ionic radii of the A, B and X ions, respectively.

Alexander *et al.*[42] analyzed 170 A_2BX_6 compounds from the ICSD database and identified an optimal range based on these two geometric factors that is applicable to double perovskite

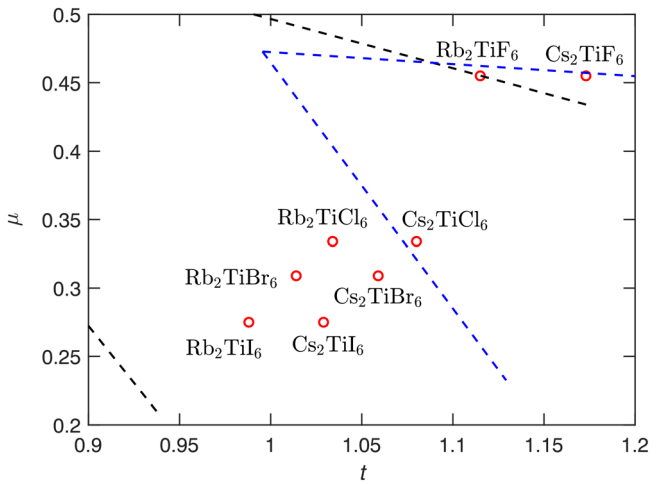

Fig. 7 Calculated Goldschmidt tolerance factor t and octahedral factor μ of A_2TiX_6 (A= Rb, Cs, X = F, Cl, Br, I). The black and blue dashed lines represent the approximate stability boundaries for double perovskite of all halides and only fluorides, respectively, as defined by Alexander *et al.*[42] The region defined by the blue dashed lines extends slightly beyond the black area because, when delineating the region based on fluorides, the starting point selection differs, resulting in a more divergent region.

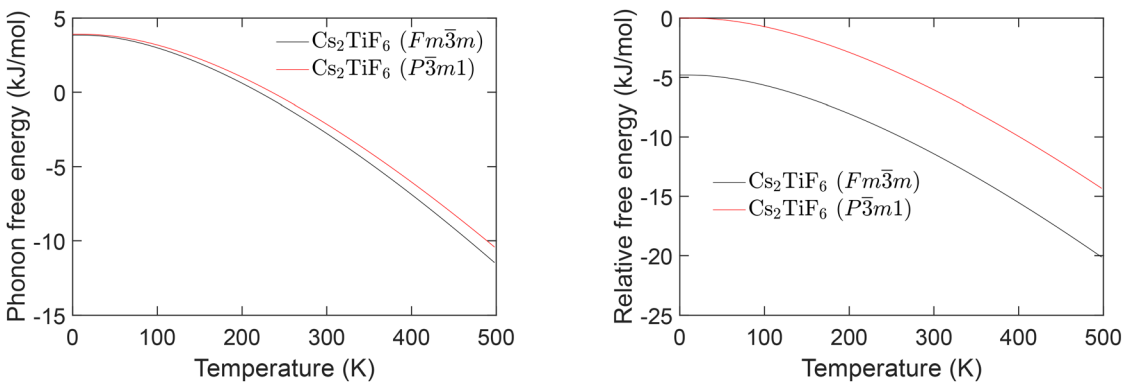

Fig. 6 Phonon free energy (left) and relative free energy (right) of Cs_2TiF_6 in two phases.

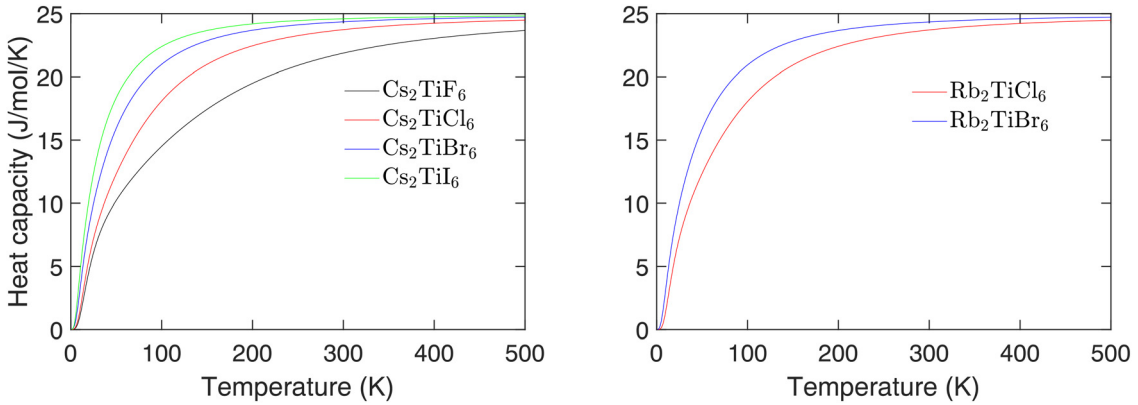

Fig. 8 Calculated heat capacities of Cs_2TiX_6, X = F, Cl, Br, I (left) and for Rb_2TiX_6, X = Cl, Br (right).

structures, within which most cubic perovskites are located. In this work, t and μ are calculated for the eight compounds studied here and compared with the optimal range proposed in that study. The effective ionic radii used in the calculations are taken from Shannon,[46] and the results are shown in (Fig. 7). It can be seen that both Rb_2TiF_6 and Cs_2TiF_6 lie near the proposed stability boundary, regardless of whether the area is defined by considering all halides or fluorides alone. This is consistent with the fact that these two can crystallize in $P\bar{3}m1$ phase, even though the cubic phase of Cs_2TiF_6 is dynamically stable and has lower free energy than its trigonal structure in our calculations. In fact, A_2BF_6 compounds may exist as multiple polymorphs.[47–49] The formation energies among these different phases are very close, as confirmed by calculations in Section 3.6. A vacancy double perovskite phase might be possible for A_2BF_6, yet it may not correspond to the minimum free energy. Its stability cannot be fully determined by the two structural factors alone. On the other hand, although Rb_2TiI_6 falls within the proposed range, the region defined by Alexander *et al.* also contains some of disordered and non perovskite compounds. This range is defined to encompass cubic perovskites, and compared with other compositions, Rb_2TiI_6 already lies closer to the boundary.

3.6 Possible space groups

The unstable phonon modes observed in Rb_2TiF_6 and Rb_2TiI_6 indicate the structures tend to distort towards lower symmetry. Since $P\bar{3}m1$ is not a subgroup of $Fm\bar{3}m$, the possible phases can be identified using the tables of Stokes and Hatch.[50,51] Based on the unstable modes at the Γ and X points shown in Fig. 2 and Fig. S3, six candidate space groups ($C2/m$, $R\bar{3}$, $P\bar{1}$, $P4_2/nnm$, $Pn\bar{3}$ and $Pnnn$) that preserve the chemical composition for each of Rb_2TiF_6 and Rb_2TiI_6 are identified. The parent $Fm\bar{3}m$ structure is then distorted according to the symmetry constraints of each candidate space group and subsequently fully relaxed. Phonon calculations at the Γ point are performed for all relaxed structures. It was found that, for both Rb_2TiF_6 and Rb_2TiI_6, only the $C2/m$ phase has no imaginary phonon frequencies at this point.

To further assess the relative stability of the distorted phases, lattice energies were also calculated. In Rb_2TiF_6, the lattice energy of the $C2/m$ phase is lower than that of the $Fm\bar{3}m$ phase by 3.59 kJ mol^{-1}, while in Rb_2TiI_6 the corresponding value is 9.83 kJ mol^{-1}. This result demonstrates that, in terms of lattice energies, the monoclinic $C2/m$ phase is also favoured over the cubic structure.

3.7 Heat capacity

For completeness, we show the calculated heat capacities of the members of the family with fully-stable phonons in Fig. 8. For A = Cs we can show results for all four types of anion X, but for A = Rb we can only show results for the two compounds that have stable phonons. The graphs show the expected trends, with faster rises on heating for the heavier X anions reflecting the lower frequencies as seen in the dispersion curves. The heat capacity for the two compounds Rb_2TiCl_6 and Rb_2TiBr_6 look very similar to the corresponding case for A= Cs, reflecting the greater importance of the X anion over the A cation in determining the dynamic properties.

4 Conclusion

We have compared the lattice dynamics and crystal stabilities of the family of materials of formula A_2TiX_6, with A = Rb or Cs, and X = F, Cl, Br or I, all with the vacancy double perovskite structure of space group $Fm\bar{3}m$. The lattice dynamics are ordered in the same way in each structure, with the lowest energy modes corresponding to rotations of the TiX_6 octahedra, immediately below the external modes involving motions of the A cations and whole-body displacements of the TiX_6 octahedra. Above these modes are the bond-bending internal modes of the TiX_6 octahedra, and at the highest frequencies are the symmetric and antisymmetric Ti–X stretching modes. The gaps between these different types of modes increases in a consistent manner with decreasing mass of the X anion. The phonon dispersion curves for both A = Rb and or A = Cs are very similar, with largest differences being in the external modes, although not always just through a simple scaling by mass.

We found that the phonons are stable in all but two cases, namely Rb_2TiF_6 and Rb_2TiI_6, where the rotational modes show instabilities at the Γ point and along the whole of the lines in reciprocal space in the [100] directions. We also showed that for Rb_2TiF_6, the $Fm\bar{3}m$ phase has a higher free energy than that of the experimentally-observed phase with space group $P\bar{3}m1$, thereby explaining why Rb_2TiF_6 always crystallises in this latter phase. Cs_2TiF_6 can also be crystallised with the $P\bar{3}m1$ structure, but we found that the free energy of the $Fm\bar{3}m$ phase is lower at all temperatures. Based on the tables of Stokes and Hatch,[50,51] we also explored the possible phases from the soft modes of the cubic $Fm\bar{3}m$ structure in Rb_2TiF_6 and Rb_2TiI_6, and found that the monoclinic $C2/m$ phase might be the stable state in both cases.

The materials of general formula A_2TiX_6 with a structure of vacancy double perovskite are among a group of materials that have been suggested might be potential new electronic ceramics as alternatives to lead-based perovskites. As such there has been much work on synthesis and characterisation, and prior DFT calculations have focused on the electronic properties and band structure, with little attention paid to their lattice dynamics. Lattice dynamics calculations underpin issues such as phase stability and thermodynamics properties. Systematic studies across a range of chemical compositions are useful for gaining understanding and insight into these matters. In the case of A_2TiX_6 we have understood the trends with changing both ions for the higher-frequency internal modes. For the external modes, and particularly the lowest-frequency rotational mode, we see trends across the range of compositions but these trends do not follow from simple scalings with mass.

Author contributions

Junbiao Guo: investigation; methodology; validation; writing (original draft); writing (review & editing); visualization. Keith Refson: software; writing (review & editing). Martin T. Dove: investigation; methodology; validation; writing (original draft); writing (review & editing); visualization.

Conflicts of interest

There are no conflicts to declare.

Data availability

The main CASTEP code is available for academic use. Information is available from https://www.castep.org/get_castep. Input and output files for the calculations, and scripts for the analysis, are available upon request.

Supplementary information (SI) contains phonon dispersion curves for 6 of the compounds, diagrams of mode eigenvectors, and a table of phonon frequencies at zero wave vector for all materials. See DOI: https://doi.org/10.1039/d5cp04058b.

Acknowledgements

We acknowledge the financial support from National Natural Science Foundation of China, grant numbers 12174274 and 12350710177, from the Joint Fund of Bijie City and Guizhou University of Engineering Science (Bijie Science and Technology Union Contract [2026] number 2), and from Guizhou Provincial Innovation Talent Workstation (KXJC (2025)044 - Qiankehe Platform) (MTD).

References

1 D. C. Palmer, *Z. Kristallogr. Cryst. Mater.*, 2015, **230**, 559–572.
2 A. Babayigit, A. Ethirajan, M. Muller and B. Conings, *Nat. Mater.*, 2016, **15**, 247–251.
3 M. Awais, R. L. Kirsch, V. Yeddu and M. Saidaminov, *ACS Mater. Lett.*, 2021, **3**, 299–307.
4 A. D. Jodlowski, D. Rodriguez-Padron, R. Luque and G. de Miguel, *Adv. Energy Mater.*, 2018, **8**, 1703120.
5 F. Igbari, Z.-K. Wang and L.-S. Liao, *Adv. Energy Mater.*, 2019, **9**, 1803150.
6 R.-I. Biega, Y. Chen, M. R. Filip and L. Leppert, *Nano Lett.*, 2023, **23**, 8155–8161.
7 L. A. Muscarella and E. M. Hutter, *ACS Energy Lett.*, 2022, **7**, 2128–2135.
8 M. R. Filip, S. Hillman, A. A. Haghighirad, H. J. Snaith and F. Giustino, *J. Phys. Chem. Lett.*, 2016, **7**, 2579–2585.
9 K. Chakraborty, N. R. Medikondu, P. B. Kanakavalli, V. V. Kamesh, S. Das, M. G. Choudhury and S. Paul, *Phys. Scr.*, 2024, **99**, 105554.
10 B. A. Connor, L. Leppert, M. D. Smith, J. B. Neaton and H. I. Karunadasa, *J. Am. Chem. Soc.*, 2018, **140**, 5235–5240.
11 X. Du, D. He, Y. Liu and N. Cheng, *J. Appl. Phys.*, 2020, **128**, 235110.
12 B. Cucco, G. Bouder, L. Pedesseau, C. Katan, J. Even, M. Kepenekian and G. Volonakis, *Appl. Phys. Lett.*, 2021, **119**, 181903.
13 M.-G. Ju, M. Chen, Y. Zhou, H. F. Garces, J. Dai, L. Ma, N. P. Padture and X. C. Zeng, *ACS Energy Lett.*, 2018, **3**, 297–304.
14 S. R. Kavanagh, C. N. Savory, S. M. Liga, G. Konstantatos, A. Walsh and D. O. Scanlon, *J. Phys. Chem. Lett.*, 2022, 10965–10975.
15 H. Albalawi, B. Ul Haq, G. Nazir, T. Ghrib, N. A. Kattan, Q. Mahmood, A. Aljameel, I. M. Morsi and S. Bouzgarrou, *Mater. Today Commun.*, 2022, **32**, 104106.
16 R. L. Lister and S. N. Flengas, *Can. J. Chem.*, 1963, **41**, 1548–1551.
17 Q. Mahmood, T. H. Flemban, H. Althib, T. Alshahrani, M. G. B. Ashiq, B. Ul Haq, Y. Tahir, A. Surrati, N. A. Kattan and A. Laref, *J. Mater. Res. Technol.*, 2020, **9**, 13043–13053.
18 J. Wei, J. Wu, Y. Wang, Y. Zhang, Z. Ma, C. Qiao and H. Zeng, *Mater. Adv.*, 2023, **4**, 3767–3773.
19 D. Kong, D. Cheng, X. Wang, K. Zhang, H. Wang, K. Liu, H. Li, X. Sheng and L. Yin, *J. Mater. Chem. C*, 2020, **8**, 1591–1597.

20 S. Aslam, A. S. Farooqi, M. Y. Abd Rahman and S. A. M. Samsuri, *Phys. Status Solidi A*, 2022, **219**, 2100671.
21 G. K. Grandhi, A. Matuhina, M. Liu, S. Annurakshita, H. Ali-Loytty, G. Bautista and P. Vivo, *Nanomaterials*, 2021, **11**, 1458.
22 E. Reyes-Francis, C. Echeverria-Arrondo, D. Esparza, T. Lopez-Luke, T. Soto-Montero, M. Morales-Masis, S.-H. Turren-Cruz, I. Mora-Sero and B. Julian-Lopez, *Chem. Mater.*, 2024, **36**, 1728–1736.
23 D. Liu, G. Yao, S. Jin, J. Chen, B. Lou, Q. Li and R. Sa, *J. Phys. Chem. Solids*, 2021, **150**, 109852.
24 S. M. Liga and G. Konstantatos, *J. Mater. Chem. C*, 2021, **9**, 11098–11103.
25 Q. Zhou, Y. Zhou, Y. Liu, Z. Wang, G. Chen, J. Peng, J. Yan and M. Wu, *J. Mater. Chem. C*, 2015, **3**, 9615–9619.
26 I. M. Shlyapnikov, E. A. Goreshnik and Z. Mazej, *Inorg. Chem.*, 2018, **57**, 1976–1987.
27 J. E. Ingall, E. Linscott, N. Colonna, A. J. Page and V. J. Keast, *J. Phys. Chem. C*, 2024, **128**, 9217–9228.
28 Q. Mahmood, M. Hassan, N. Yousaf, A. A. AlObaid, T. I. Al-Muhimeed, M. Morsi, H. Albalawi and O. A. Alamri, *Mater. Sci. Semicond. Process.*, 2022, **137**, 106180.
29 M. Chen, M.-G. Ju, A. D. Carl, Y. Zong, R. L. Grimm, J. Gu, X. C. Zeng, Y. Zhou and N. P. Padture, *Joule*, 2018, **2**, 558–570.
30 J. Euvrard, X. Wang, T. Li, Y. Yan and D. B. Mitzi, *J. Mater. Chem. A*, 2020, **8**, 4049–4054.
31 J. L. Mendes, W. Gao, J. L. Martin, A. D. Carl, N. A. Deskins, S. Granados-Focil and R. L. Grimm, *J. Phys. Chem. C*, 2020, **124**, 24289–24297.
32 S. J. Clark, M. D. Segall, C. J. Pickard, P. J. Hasnip, M. I. J. Probert, K. Refson and M. C. Payne, *Z. Kristallogr. Cryst. Mater.*, 2005, **220**, 191–194.
33 J. P. Perdew, K. Burke and M. Ernzerhof, *Phys. Rev. Lett.*, 1996, **77**, 3865–3868.
34 J. P. Perdew, K. Burke, M. Ernzerhof and R. Ernstorfer, *Phys. Rev. Lett.*, 1997, **78**, 1396.
35 H. J. Monkhorst and J. D. Pack, *Phys. Rev. B*, 1976, **13**, 5188–5192.
36 S. Baroni, S. de Gironcoli and A. D. Corso, *Rev. Mod. Phys.*, 2001, **73**, 515–562.
37 K. Refson, P. R. Tulip and S. J. Clark, *Phys. Rev. B: Condens. Matter Mater. Phys.*, 2006, **73**, R4954–12.
38 W. Stirling, *J. Phys. C: Solid State Phys.*, 1972, **5**, 2711–2730.
39 A. Giddy, M. Dove, G. Pawley and V. Heine, *Acta Crystallogr., Sect. A*, 1993, **49**, 697–703.
40 L. Tan, V. Heine, G. Li and M. T. Dove, *Rep. Prog. Phys.*, 2024, **87**, 126501.
41 J. Zhou, Y. Wang, Y. Chen, Y. Zhou, B. Milicevic, L. Zhou, J. Yan, J. Shi, R.-S. Liu and M. Wu, *Angew. Chem., Int. Ed.*, 2021, **60**, 3940–3945.
42 A. E. Fedorovskiy, N. A. Drigo and M. K. Nazeeruddin, *Small Methods*, 2020, **4**, 1900426.
43 V. Goldschmidt, *Naturwissenschaften*, 1926, **14**, 477–485.
44 M. Lufaso and P. Woodward, *Acta Crystallogr., Sect. B: Struct. Sci., Cryst. Eng. Mater.*, 2004, **60**, 10–20.
45 C. Li, K. Soh and P. Wu, *J. Alloys Compd.*, 2004, **372**, 40–48.
46 R. Shannon, *Acta Crystallogr., Sect. A*, 1976, **32**, 751–767.
47 L. Smrcok, A. Le Bail, M. Boca and A. Rakhmatullin, *Cryst. Growth Des.*, 2020, **20**, 3867–3881.
48 G. Benner and R. Hoppe, *J. Fluorine Chem.*, 1990, **48**, 219–227.
49 C. Hebecker, H. G. Vonschne and R. Hoppe, *Naturwissenschaften*, 1966, **53**, 154.
50 H. T. Stokes, D. M. Hatch and B. J. Campbell, *ISOSUBGROUP, ISOTROPY Software Suite*, https://iso.byu.edu.
51 H. T. Stokes, S. van Orden and B. J. Campbell, *J. Appl. Crystallogr.*, 2016, **49**, 1849–1853.